

# From Ultracompact to Extended H II Regions. II : Cloud Gravity and Stellar Motion

José Franco<sup>1</sup>

*Instituto de Astronomía-UNAM, Apdo Postal 70-264, 04510 México D.F., Mexico*

Guillermo García-Segura<sup>2</sup>

*Instituto de Astronomía-UNAM, Apdo Postal 877, 22800 Ensenada, Baja California, Mexico*

Stanley E. Kurtz<sup>3</sup>

*Centro de Radioastronomía y Astrofísica-UNAM, Apdo Postal 3-72 (Xangari), 58089 Morelia, Michoacán, Mexico*

## ABSTRACT

The dynamical evolution of H II regions with and without stellar motion in dense, structured molecular clouds is studied. Clouds are modeled in hydrostatic equilibrium, with gaussian central cores and external halos that obey power laws as  $\rho \propto r^{-2}$  and  $\rho \propto r^{-3}$ . The total pressures at the core centers are  $P/k = 10^9 \text{ K cm}^{-3}$ . The cloud gravity is included in a simplified manner as a time-independent, external force. Stellar velocities of 0, 2, 8, and 12 km s<sup>-1</sup> are considered; all are less than the equilibrium dispersion velocity of the cloud (13 km s<sup>-1</sup>). When stellar motion is included, stars move from the central core to the edge of the cloud, producing transitions from ultracompact to extended H II regions as the stars move into lower density regions. The opposite behavior is also feasible when stars move toward the cloud cores. The main conclusion of our study is that ultracompact H II regions are pressure-confined entities while they remain embedded within dense cores. The confinement comes from either ram or ambient pressures, or a combination of both. The survival of ultracompact regions (by definition  $\lesssim 0.1 \text{ pc}$ ) depends on the position of the star with respect to the core center, the stellar life-time, and the crossing time of the cloud core. Stars with velocities less than the cloud dispersion velocity can produce cometary shapes with sizes under 0.1 pc at evolutionary times of  $2 \times 10^4 \text{ yr}$  or greater, in statistical agreement with observations. The sequence Ultracompact H II  $\rightarrow$  Compact H II  $\rightarrow$  Extended H II shows a rich variety of unpredictable structures due to ionization-shock front instabilities. Some

---

<sup>1</sup>Email address: pepe@astroscu.unam.mx

<sup>2</sup>Email address: ggs@astrosen.unam.mx

<sup>3</sup>Email address: s.kurtz@astrosmo.unam.mx

ultracompact H II regions with a core-halo morphology could be explained by self-blocking effects, when stars overtake and ionize leading, piled-up clumps of neutral gas. Because of computational restrictions, we use thermal energy to support the cloud against gravity; the results remain the same if other types of isotropic cloud support are used, such as hydrodynamic or turbulent pressure.

*Subject headings:* Hydrodynamics — ISM: clouds — H II regions

## 1. Introduction

The classical picture of H II regions presents the idea of a newly-formed massive star that begins to produce large quantities of UV photons and hence to ionize the surrounding medium. If the star is still embedded within the molecular cloud from which it formed, then the molecular gas will dissociate and ionize, and an ionization front will form, expanding rapidly outward to form the initial Strömgren sphere. The ionization front expands very rapidly at first, but soon slows, and approaches the sound speed after a few recombination times. The newly ionized gas will be greatly over-pressured with respect to the original molecular gas and, in the classical picture, will expand toward pressure equilibrium with its environment. In pressure equilibrium, for ionized gas velocity dispersion  $c_i$  and initial (molecular) cloud velocity dispersion  $c_0$ , the final radius can be expressed in terms of the initial Strömgren radius,  $R_s$ , as

$$R_f = R_s \left( \frac{c_i^2}{c_0^2} \right)^{2/3}. \quad (1)$$

For typical values of  $c_i$  and  $c_0$ , one expects the final radius to be nearly 100 times its initial value. The strong shock approximation for the expansion gives the Strömgren sphere radius as a function of time (Spitzer 1954)

$$R_{HII} \simeq R_S \left( 1 + \frac{7}{4} \frac{c_i t}{R_S} \right)^{4/7}. \quad (2)$$

Adopting  $c_i = 10 \text{ km s}^{-1}$  as the sound speed, and assuming a factor of 100 expansion, implies that the H II region will reach pressure equilibrium in a time longer than  $3 \times 10^6$  years. (Equation 2 provides an upper bound because the dynamical evolution departs from the strong shock approximation as the expansion velocity decreases.) At this time it will have a radius of about one parsec. The basic physical processes relevant for the detailed structure and expansion of H II regions are discussed extensively in Osterbrock (1989). Other important considerations driving the formation and expansion phases are discussed in Franco, Tenorio-Tagle & Bodenheimer (1990). The salient point here is that the general scheme outlined above for the expansion of recently formed H II regions is problematic, in that it predicts that the region will rapidly expand out of its initial, small, dense (ultracompact) state. In particular, adopting 0.1 pc as the nominal size for an ultracompact

(UC) H II region, one expects the lifetime of this phase to be of order  $r/c_i$ , or about  $10^4$  yr. Many more UC HII regions are seen than this naive view predicts, hence the conclusion is that their lifetimes must be longer than anticipated by this simple theory.

During the past decade various attempts have been made to address this so-called “lifetime problem” (see Garay & Lizano 1999, Kurtz et al. 2000, and Churchwell 2002 for reviews). These attempts can be divided into two categories: those which prolong the life by providing a confining force, and those which extend the life by adding a mass source, thus replenishing the ionized gas. In both cases, however, the net result of the process is that the pressure of the ionized region is increased, leading to densities and sizes comparable to those observed in UC H II regions for extended periods of time.

Attempts to prolong UC H II region lifetimes by providing an additional confining force include the bow-shock model (Van Buren & McCray 1988; Van Buren et al. 1990; Mac Low et al. 1991; Van Buren & Mac Low 1992), using thin-shell solutions for the bow-shock computation. These models concluded that UC H II regions could be confined by ram pressure when they travel through a cloud. García-Segura & Franco (1996, hereafter, paper I) showed that other sources of pressure may also play an important role. For example, thermal pressure within a cloud core can itself confine a UC H II region to small sizes, as suggested by De Pree, Rodríguez & Goss (1995). It seems unlikely, however, that the simple action of thermal pressure can give rise to the variety of observed morphologies, and additional ways of increasing the total pressure have been explored. For instance, one can achieve this by replenishing the ionized gas. Hollenbach et al. (1994), Yorke & Welz (1996), and Richling & Yorke (1997) modeled UC H II regions resulting from the photo-evaporation of circumstellar disks, while Dyson, Williams, & Redman (1995) and Lizano et al. (1996) modeled them as photo-evaporating clumps. A key result of all these studies is the realization that the “compactness” (i.e., the small diameter and high density) of the HII region may not be a good indicator of its youthfulness.

Following along these lines, in this paper we discuss models that include stellar motions, and combine the effects of ram and thermal (or other) pressures. Again, as in Paper I, we use thermal pressure as an illustration of the impact that *any* isotropic pressure may have on the dynamical evolution of H II regions. Here we present gas dynamical simulations that complement those of paper I. The inclusion of stellar motion introduces a preferential direction for the pressure variation and gives rise to a variety of different situations as the stars leave their parental cloud cores and evolve into extended H II regions. A wide variety of shapes is encountered for extended H II regions, and we confirm the appearance of saw-tooth ionization-shock fronts discussed in paper I and Williams (2002).

Another aspect considered in this paper is that H II regions are calculated off-center from their parental clouds. Previous studies (i.e., Franco et al. 1990 and references therein) considered stars located at the peak of the density structures, and the solutions for the expansion assumed spherical symmetry from the core center. In the off-center cases, and for the core densities used

here ( $\sim 10^7 \text{ cm}^{-3}$ ), a large number of ionizing photons is required for complete core ionization and our simulations admit the possibility that the outer core material either remains un-ionized or recombines at a late evolutionary stage.

Section 2 gives an observational background from recent radio studies. §3 describes the model and the assumptions made. §4 explains and shows the gas dynamical simulations, and §5 discusses the results and gives our conclusions.

## 2. Observational Background

The physical properties of H II regions span orders of magnitude in scale. The classes most closely linked to star formation are the smallest, densest, and (possibly) youngest stages: the compact, ultracompact, and hypercompact HII regions. Compact H II regions were first identified as such by Mezger et al. (1967), who characterized them as having sizes from 0.06 to 0.4 pc and electron densities around  $10^4 \text{ cm}^{-3}$ . The smallest and densest of these came to be known as ultracompact H II regions. By the mid-1980s around a dozen of these UC H II regions were known. The situation changed dramatically with the survey of Wood & Churchwell (1989) which identified over 70 UC H II regions. Further surveys carried out by Becker et al. (1994), Kurtz, Churchwell & Wood (1994), Walsh et al. (1998), and Gieveon et al. (2005) identified many more, and at present the number of probable ultracomacts is of order 1000. These regions are (observationally) defined as having sizes  $\lesssim 0.1 \text{ pc}$  and densities  $\gtrsim 10^4 \text{ cm}^{-3}$ . The surveys revealed that UC H II regions present a variety of morphological types, including cometary, core-halo, shell, spherical, and multiply-peaked (see Wood & Churchwell 1989, Fig. 143). A modification to this morphological scheme, including the addition of a bipolar morphology, has been suggested by De Pree et al. (2005). Hypercompact H II regions, only recently recognized as a distinct class (e.g., Sewilo et al. 2004), are even smaller and denser than UC H II regions, but so far are fairly rare, with only about a dozen presently known.

Most of the radio surveys mentioned above suffered from the observational bias that they were insensitive to regions larger than about  $30''$ . This bias arises from the nature of interferometric observations, which are sensitive only to a range of angular sizes, determined by the range of baseline lengths. Although some lower resolution studies exist (e.g., Garay et al. 1993), the larger UC H II region surveys were made with arc second or better angular resolution. For the radio interferometers used in these surveys (the VLA and the ATCA) this implies observations that are insensitive to structures larger than approximately  $30''$ .

Low resolution observations of UC H II regions indicate that this observational bias may result in a significant misrepresentation of some regions. Kurtz et al. (1999) and Kim & Koo (2001) made low resolution VLA observations of UC H II regions from the Kurtz et al. (1994) and the Wood & Churchwell (1989) surveys, respectively, and found that a large fraction had extended free-free emission surrounding the ultracompact components. The physical relationship between the

extended and the compact components is unclear; the evidence for a relationship is morphological in most cases. Kim & Koo report radio recombination line observations which support the hypothesis of a relation based on close agreement of the line velocities between the ultracompact and extended components.

The presence of the extended component surrounding the ultracompact component has been known since the seminal work of Mezger et al. (1967). Since that time attention has focused on the ultracompact component and relatively little has been done to explore what role the extended gas plays in the dynamics of the UC H II regions. Further observational work is needed in this area to confirm the relationship between the compact, high density gas and the extended, low density gas. If confirmed, there will be a number of ramifications for our understanding of UC H II regions. First, the stellar content of the H II regions (i.e., the ionizing photon flux) will have to be revised upward to account for the much greater ionized mass. Second, the theoretical models currently proposed will have to account for the extended emission. Although the best-known HII region, Orion, has ionized gas ranging from  $n_e$  of about  $400 \text{ cm}^{-3}$  to over  $10^5 \text{ cm}^{-3}$  (Felli et al. 1993); none of the currently proposed UC HII models can easily explain the coexistence of such different densities.

A general scheme that could give rise to a wide range of ionized gas densities was suggested by Franco et al. (2000), and shown pictorially in Figure 8 of Kim & Koo (2001). Using the free-free radio-continuum spectral index of three UC and hypercompact H II regions, Franco et al. (2000) found that the ionized gas emission can be fit by power-law density distributions with exponents between  $-2$  and  $-4$ . These are rather steep gradients, the more extreme cases being significantly steeper than the gradients found in molecular line studies of star-forming clouds (which show exponents between  $-1.5$  and  $-2$ , typical of equilibrium isothermal clouds). The reasons for this behavior are unclear. As Franco et al. point out, the extreme value derived (close to  $-4$ ) may be an over-estimate of the actual density gradient. Despite our lack of understanding of the nature and maintenance of such steep gradients, here we consider clouds with power-law exponents of  $-2$  and  $-3$ . The suggestion, then, is that the density gradients and range of structured scale sizes in molecular clouds may give rise to compact and extended structures when ionized by the nascent stars. The present article is an attempt to develop this model in a quantitative way.

### 3. Initial considerations

We assume a cloud consisting of an internal core of radius  $r_c$  and a halo in hydrostatic equilibrium, with a constant total velocity dispersion ( $P = \rho c_0^2$ , and  $c_0 = \text{constant}$ ),

$$\vec{\nabla} P = -\rho \vec{g} \Rightarrow \vec{\nabla} \rho = -\frac{\rho}{c_0^2} \vec{g}. \quad (3)$$

For simplicity, due to computational restrictions, we assume that the gas is always described by a single equation of state and the total velocity dispersion is set equal to the isothermal sound

speed,  $c_s$ . Thus, the resulting *effective* temperature is representative of the kinetic energy required to provide support against gravity, and is well above any actual molecular cloud temperature (i.e., the contribution from turbulent pressure is included in an implicit manner). Assuming that the cloud is spherically symmetric ( $\vec{\nabla} \rightarrow \frac{d}{dr}$  and  $\vec{g} \rightarrow g_r$ ), we solve only along the radial coordinate:

$$\frac{d\rho}{dr} = - \frac{\rho}{c_s^2} g_r . \quad (4)$$

For the first set of simulations (designated model A) we assume that the halo density falls off as an  $r^{-2}$  power law, as in a self-gravitating isothermal cloud:

$$\rho(r) = \rho_c (r/r_c)^{-2} \quad \text{for } r \geq r_c . \quad (5)$$

Solving for  $g_r$  with equations 4 and 5, we find

$$g_r = \frac{2 c_s^2}{r} = \frac{2 c_s^2}{r_c} (r/r_c)^{-1} \quad \text{for } r \geq r_c . \quad (6)$$

Inside the core,  $g_r$  must grow from zero up to  $2 c_s^2/r_c$ . A simple way to achieve this is to let  $g_r$  grow linearly within the core, as  $g_r = A (r/r_c)$ . In order to join the halo solution (equation 5), we require that  $A = 2 c_s^2/r_c$ .

The density distribution inside the core is found by integrating equation 4 with the new  $g_r$ , giving

$$\rho(r) = \rho_0 \exp \left[ - (r/r_c)^2 \right] \quad \text{for } r \leq r_c , \quad (7)$$

where  $\rho_0$  is the central density at  $r = 0$ , and  $\rho_c = \rho_0/e$ .

In summary, the density distribution of the cloud is given by

$$\rho(r) = \begin{cases} \rho_0 \exp \left[ - (r/r_c)^2 \right] & \text{for } r \leq r_c \\ \rho_0/e (r/r_c)^{-2} & \text{for } r \geq r_c \end{cases} \quad (8)$$

and the gravitational acceleration by

$$g_r = \begin{cases} 2 c_s^2/r_c (r/r_c) & \text{for } r \leq r_c \\ 2 c_s^2/r_c (r/r_c)^{-1} & \text{for } r \geq r_c . \end{cases} \quad (9)$$

For the second set of simulations (designated model B) we assume that the halo density falls off as an  $r^{-3}$  power law, and using the above approach we find the density distribution

$$\rho(r) = \begin{cases} \rho_0 \exp \left[ -3/2 (r/r_c)^2 \right] & \text{for } r \leq r_c \\ \rho_0/e^{3/2} (r/r_c)^{-3} & \text{for } r \geq r_c \end{cases} \quad (10)$$

and the gravitational acceleration

$$g_r = \begin{cases} 3 c_s^2/r_c (r/r_c) & \text{for } r \leq r_c \\ 3 c_s^2/r_c (r/r_c)^{-1} & \text{for } r \geq r_c . \end{cases} \quad (11)$$

For both sets of simulations we assume that the star was born *in situ*, inside the core of its parental cloud (modeling of “run-away” stars is not considered). The largest expected stellar velocity that such a cloud can produce is given by the dispersion velocity in hydrostatic equilibrium. Noting that (see §2.1 in paper I)  $P = 16/9 \pi G \rho_c^2 r_c^2 = \rho_c c_s^2$ , and solving for  $c_s$ , we find

$$c_s = 4.07 r_{0.1} n_6^{1/2} \text{ km s}^{-1} \quad (12)$$

where  $r_{0.1}$  is the core radius in units of 0.1 pc and  $n_6$  the core density in units of  $10^6 \text{ cm}^{-3}$ . Thus, for core densities of  $10^7 \text{ cm}^{-3}$  and radii of 0.1 pc, stellar velocities up to  $\sim 13 \text{ km s}^{-1}$  can be considered.

#### 4. 2-D gas dynamical simulations

The numerical simulations are performed with the gas dynamical MHD code ZEUS-3D version 3.4 (Stone & Norman 1992; Clarke 1996; see paper I for details). We use Cartesian coordinates with the Y-axis being the symmetry axis (i.e., a slab geometry). Thus, the star can be placed anywhere in the X-Z plane. This is a particularly safe choice because it does not introduce any axis artifact in the computations (as would cylindrical coordinates).

The set-up is similar for all models: the star is fixed on the computational mesh and remains at the same location during the computation. The stellar motion is simulated by setting the gas to a single speed throughout the mesh. As the simulation proceeds, the outer boundary of the Z-axis is updated with the incoming gas at the stellar velocity. This update depends on the nature of the problem and accounts for the change in the cloud density distribution as a function of position. In reality, the situation is far more complicated because the velocity is also a function of time: the stellar velocity changes as it moves through the gravitational potential of the cloud but, unfortunately, this variation cannot be included here in a self-consistent manner. All models have the same numerical resolution of 250 zones along both the X and Z axes.

We use the same approach as paper I to model the H II region (see Bodenheimer, Tenorio-Tagle & Yorke 1979), i.e., we solve a radial integral to find the position of the ionization front (Strömgren 1939). The temperature inside the H II region is set to  $10^4 \text{ K}$ , the approximate photoionization equilibrium temperature.

The modeling of a “realistic” UC H II region includes a hypersonic stellar wind (i.e., an ultracompact bubble) and is very expensive in computational time, owing to the fact that the wind speeds from massive main sequence stars are of order  $10^3 \text{ km s}^{-1}$  when their bubble sizes are of order  $10^{-2} \text{ pc}$ . This forces the Courant condition to calculate very small time-steps during the simulations. Thus, it is possible to include stellar winds in 2-D simulations that cover physical times of order  $10^3 \text{ yr}$ , but this is very time consuming when the required physical times are of order  $10^5 \text{ yr}$ . For this reason, we do not include the effects of the stellar wind in the present models. Nonetheless, Paper I showed that at these high densities the size of the UC H II region is primarily

determined by the gas pressure. Thus, our results can be considered qualitatively correct.

To begin our study we computed several cases (not shown here) in which the star was located at the center of the core (given by equation 8) and had zero velocity. For a core radius of 0.1 pc, a central density of  $10^7 \text{ cm}^{-3}$  and an ionizing photon flux of  $F_\star = 10^{48} \text{ s}^{-1}$ , the models followed similar tracks as those described in the 1-D solutions of Paper I. This is understandable, because the gaussian core described by equation 8 produces a central plateau which resembles the constant density medium used in the first part of Paper I. Thus, pressure equilibrium is achieved on timescales matching those of Paper I. The novel aspect here is the inclusion of gravity, which affects the final density structure. This is illustrated in the next paragraph.

A second set of models, also without stellar motion (models A0 and B0; see Table 1), are calculated with the star at the edge of the core (Figure 1a). The purpose of these models is to study the expansion and dynamics of the H II regions in the two different density ramps given by equations 8 and 10 for  $r \geq r_c$ . Model A0 is shown in detail in Figure 1b, while model B0 is shown in Figure 1c. The ionized gas has a flat density distribution during the first forty thousand years (first two curves) in both cases. But as the evolution proceeds, the ionized gas – subject to the cloud gravity – adjusts its density distribution to come into hydrostatic equilibrium. This is clearly seen in model A0, where pressure equilibrium is achieved (curves 7 – 10) and the final density distribution follows the initial density ramp. The final density is a factor of 200 lower, however, because the gas was originally at  $10^2 \text{ K}$  but hydrostatic equilibrium is achieved at  $10^4 \text{ K}$ . In contrast, model B0 does not reach pressure equilibrium in the computational domain, and a blister-like region or champagne flow (Tenorio-Tagle 1979) is produced. Gas is permanently photo-evaporated from the cloud, resulting in a steady-state mass loss. As a result, the final solution is closer to an  $r^{-2}$  profile than to the original  $r^{-3}$  density ramp.

We note that the density ramps for these models are off-center from the stellar position; i.e., the origin of the power law does not coincide with the stellar coordinates. In addition, in some models, the star moves. As such, the spherically symmetric solutions given by Franco et al. (1990) are not directly applicable in all cases.

A third set of models (A2, A8, A12 and B2, B8, B12) include stellar motion at 2, 8, and 12  $\text{km s}^{-1}$  (Table 1). In these cases the star moves from the core center toward the edge, eventually leaving the core and entering the density ramp described in equations 8 and 10. While the star is still inside the core, these models create cometary shapes arising from the leading bow-shock, with sizes typical of UC H II regions. When the star enters the density ramp, the H II region grows in size along the density gradient and drops in density. If the stellar velocity is high compared to the H II expansion velocity then the cometary shape is maintained. If the stellar velocity is low compared to the H II expansion velocity, the region quickly evolves into a blister morphology. The results of this third set of models, including a constant stellar motion, are shown graphically in Figures 2 – 6.

Figures 2 and 3 show models A2 and B2, respectively. Owing to the lower stellar velocity, four



time frames are adequate to show the evolution. In these two simulations the star is initially at the core center and moves toward  $+z$ . Our computational method leaves the star fixed at the position  $[(x, z)_* = (0.25, 0.1)]$  while the gas moves toward  $-z$  at  $2 \text{ km s}^{-1}$ . At the time of the first frame ( $0.8 \times 10^5 \text{ yr}$ ) the star has already reached the core edge and entered into the density ramp. In subsequent frames, the star has moved outward in the density ramp, leaving the cloud progressively further behind (toward  $-z$ ). The behavior of models A2 and B2 is qualitatively similar. However, owing to the steeper density gradient, model B2 grows more rapidly, showing greater expansion.

Figure 4 shows the final shape of the ionized region of models A0, B0, A2, and B2 (the final times shown for each model are different, as described in the figure caption). All four models present a cometary morphology, but in all cases the gas dynamics correspond to a champagne flow, not a bow shock. The sizes and shapes of the ionized regions are different (except for the B0 case) than those of the final cavities shown in Figures 1a, 2, and 3. This is because the density of the ionized region tends to a uniform value, washing away the initial gradient and, as a consequence, the ionization front recedes (i.e., it becomes a recombination front). Thus, the gas in the outer part of the expanding cavity recombines and cools. The pressure drops quickly in these regions, forming blobs and filaments due to thermal and dynamical instabilities. The effects are clearly noticeable in the B2 model (last frames of Figures 3 and 4).

Figure 5 shows the total (5a) and ionized (5b) gas densities for models A8 and A12. A cometary morphology is clearly evident during the first half of the evolution for both models. Unlike the A2 model, for which this morphology arose from a champagne flow, the higher velocities of the A8 and A12 models result in bow shocks. During the second half of the evolution, as the star moves into much lower density gas, the cometary arc opens substantially. Also, instabilities in both the ionization and shock fronts, as those described in Paper I and Williams (2002), create complex structures with finger-like condensations that resemble elephant trunks (see also Williams et al. 2001). Indeed, it is not clear that at late times these ionized regions would even be recognized as being cometary. Corresponding time frames between the A8 and A12 models show that the H II region has evolved to a larger size for the A12 model than the A8 model. This is because the higher stellar velocity of the A12 model has carried the star to a lower density region of the cloud, where the H II region can expand more freely.

Figure 6 shows the total (6a) and ionized (6b) gas densities for models B8 and B12. Compared to the A8 and A12 models, the B8 and B12 models evolve more rapidly, expanding beyond the ultracompact stage in about half the time (the time sequence shown in Figure 6 is shorter than that of Figure 5). As stated in the case of Figure 4, the ionization front is always inside the expansion cavity, and the gas recombines at several locations. Perhaps most intriguing about the B8 and B12 models is that both pass through a phase (at 52,000 yr and 40,000 yr, respectively) when distinct high density components are seen within the HII region. These high density components have sizes and densities typical of UC H II regions, but they are embedded in larger, lower density ionized gas more typical of compact H II regions. This is discussed further in §5.4.

The sequence Ultracompact H II  $\rightarrow$  Compact H II  $\rightarrow$  Extended H II shows, as stated above, a rich variety of unpredictable structures due to the I-S front instability (see paper I). Figures 5-7 show examples of how rich the development of the I-S front instability can be. The small scale structures found in the computations (Fig. 7) are always transient. The lifetime of these structures, or elephant trunks, is proportional to their mass and the size of the H II region, and inversely proportional to the stellar speed. This is because their destruction depends on the photo-evaporation rate, which in turn depends on the position and orientation of the ionizing source. The model does not purport to explain the M16 pillars, which are 50 times larger, but does suggest, as discussed in more detail by Williams et al. (2001), how their formation might occur.

## 5. Discussion and Conclusions

The results presented here show a number of important features that may be useful in understanding some of the observational puzzles of H II region evolution. Our simulations are performed with simplified models, however, and further studies with additional refinements are needed. In particular, the gravitational acceleration is treated here as a time-independent radial function, and the stellar velocity is simply set to a constant value. Obviously, both quantities are continually modified as the cloud is photo-evaporated and the star changes location in the gravitational field. Thus, a self-consistent treatment of the problem will provide better details of the evolutionary features. Also, we do not include pre-existing clumps in the cloud matter, nor large-scale vorticity in the gas velocity, which will add complexity to the resulting structures. Despite these restrictions, our results provide an adequate qualitative guideline to the effects resulting from the motion of recently formed massive stars in centrally condensed cloud cores.

### 5.1. The Star Formation Rate

The results for model A0 indicate that solutions exist in which clouds are not completely disrupted by ionization fronts; hence, star formation could proceed for longer times in those clouds. Because stellar motion is also able to confine H II regions by ram pressure in the bow shock, the ionized gas is confined within the cloud and the star formation rate of the cloud is relatively unaffected. The results are quite different for model B0, with a steep gradient, or any of the models with larger stellar velocities, ( $8 \text{ km s}^{-1}$  or above) in which the rapid expansion of the ionized gas in the lower density regions of the cloud would quickly lead to cloud destruction, thus ending the star formation phase (Franco, Shore & Tenorio-Tagle 1994; Diaz-Miller, Franco & Shore 1998).

## 5.2. Density Gradients

The results for model A0 are also interesting because if pressure equilibrium is achieved, the density gradient in the H II region will match the original density gradient of the parental cloud (see Franco et al. 2000). However, model B0 shows that molecular cloud density gradients above  $\rho \propto r^{-2}$  cannot lead to pressure equilibrium, indicating that H II region gradients obtained in these cases probably do not reflect the initial cloud conditions.

Another aspect that is important to stress is that champagne flows are transient, and in some cases they may be short-lived. Figures 1 – 4 show that, except for model B0, the initial champagne flow disappears either because the H II region reaches pressure equilibrium or the ionized gas recombines. The latter case leads to neutral outflows generated by a recombination front, as originally discussed for disk-like clouds by Franco et al. (1989). Three scenarios give rise to more-or-less steady champagne flow solutions: density gradients steeper than  $\rho \propto r^{-2}$  at the core edge; ionizing photon rates high enough to ionize the whole core; and core densities much smaller than the value used here ( $n_0 = 10^7 \text{ cm}^{-3}$ ). The latter possibility appears to be ruled out for hot molecular cores (which have densities equal to or even larger than  $10^7 \text{ cm}^{-3}$ ).

## 5.3. The Lifetime Problem and UC H II Morphologies

Any proposed solution to the lifetime problem for UC H II regions must explain how dense, compact ionized gas can remain in that state for timescales of order  $10^5 \text{ yr}$ . We find that model A0 (the stationary model with  $\rho \propto r^{-2}$ , and also the stationary 1-D model of Paper I) and models A2 and B2, (the low stellar velocity models) are able to produce UC H II regions smaller than 0.1 pc at evolutionary times larger than  $10^5 \text{ yr}$ . An additional important effect, not considered here, is UV absorption from dust grains inside the cloud cores (Diaz-Miller et al. 1998; Arthur et al. 2005). This substantially reduces the size of H II regions in dense places, and our results provide only upper limits for the sizes of the photoionized regions. This makes even easier the confinement of UC H II regions during the required time scales.

A star moving at  $1 \text{ km s}^{-1}$  will leave a 0.1 pc core in  $10^5 \text{ yr}$  (starting from the core center). The reason why solutions with  $2 \text{ km s}^{-1}$  stellar velocities are still within the range of UC H II parameters is because of ram pressure confinement. UC H II regions remain ultracompact ( $\lesssim 0.1 \text{ pc}$ ) as long as they remain inside the cloud core. In this case, the lifetime as an ultracompact region would be defined by the core crossing time. In the event that the stellar orbit never reaches the core edge, the ultracompact lifetime would be the stellar lifetime, as discussed in Paper I.

Wood & Churchwell (1989) found that the cometary and core-halo morphologies were the most common (20% and 17%, respectively, in their sample), suggesting that these morphologies have longer lifetimes than the other morphologies, thus making their detection more probable. For comparison, we find the evolutionary time for each model when the solution (still dominated by

ram pressure) reaches a size of 0.1 pc. These times (see Table 1) are: A2-B2  $\sim 8 \times 10^4$  yr, A8-A12  $\sim 6.4 \times 10^4$  yr, and B8-B12  $\sim 4 \times 10^4$  yr. The times for the higher velocity models are roughly one-third of the nominal  $10^5$  yr UC H II lifetime, consistent with the 37% of the Wood & Churchwell sample showing a cometary or core-halo morphology.

#### 5.4. The Coexistence of Compact and Extended Emission

An intriguing self-blocking effect, in which the star overtakes a leading, piled-up clump of gas and ionizes it, is seen in models B8 and B12. The effect occurs at 52,000 yr and 40,000 yr, respectively, shown in frames 4 and 11 of figure 6b. Such regions could appear in radio maps as having a core-halo morphology. Moreover, if the linear extent of the ionized gas is several tenths of a parsec or more when the self-blocking occurs, this phenomenon could appear as an ultracompact H II region coexisting with extended emission. The H II density contrast in frames 4 and 11 is about 20. For comparison, inferred values for the density contrast in the Orion H II region range from about 40 (Wilson & Jäger 1987) to nearly 600 (Felli et al. 1993), with the larger value resulting from sensitivity to small, dense clumps.

The self-blocking transients seen in models B8 and B12 depend on the resolution used; a resolution convergence study is needed to confirm the effect. This effect is not seen in models A8 or A12. This could be a result of the shallower density gradient or it could also be a result of the resolution employed. We caution that a more complete treatment of the radiative transfer could modify these results, hence we do not make any quantitative claim about the frequency of occurrence or lifetime of this morphology. We merely suggest that the core-halo or extended emission morphology might arise from self-blocking effects. This is illustrated in figure 8, where we show a contour plot of  $n_e^2$  for model B12 together with a contour image of G31.3–0.2, a UC H II region with extended emission. The model does not purport to explain the G31.3–0.2 region, which is about 30 times larger, but it does suggest how its formation might occur.

#### 5.5. Summary

To summarize, the models indicate that UC H II regions are long-lived objects while they are inside their parental cloud cores. When stars escape from these cores, transitions to larger structures, possibly UC H II regions with extended emission, are expected to occur. Conversely, stars can also fall back into the core owing to the gravitational potential of the cloud. The more extended ionized gas would recombine, leaving smaller ionized structures.

We thank Michael L. Norman and the Laboratory for Computational Astrophysics for the use of ZEUS-3D. G.G.-S. thanks the 1998 OAN summer students for the mosaic of M16 obtained with the 84 cm telescope at San Pedro Mártir. The computations were performed on the SGI Origin 2000 at IA-UNAM (Ensenada). This work has been partially supported by grants from DGAPA-UNAM

(IN130698, IN117799 & IN114199) and CONACyT (32214-E, 36568-E, & E-43121).

## REFERENCES

- Arthur, S. J., Kurtz, S. E., Franco, J., & Albarra, M. Y. 2004, *ApJ*, 608, 282
- Bodenheimer, P., Tenorio-Tagle, G., & Yorke, H. W. 1979, *ApJ*, 233, 85
- Becker, R. H., White, R. L., Helfand, D. J., & Zoonematkermani, S. 1994, *ApJS*, 91, 347
- Churchwell, E. 2002, *ARAA*, 40, 27
- Clarke, D. 1996, *ApJ*, 457, 291
- De Pree, C. G., Rodríguez, L. F., & Goss, W. M. 1995, *RevMexAA*, 31, 39
- De Pree, C. G., Wilner, D. J., Deblasio, J., Mercer, A. J., & Davis, L. E. 2005, *ApJ*, 624, L101
- Diaz-Miller, R. I., Franco, J., & Shore, S. N. 1998, *ApJ*, 501, 192
- Dyson, J. E., Williams, R. J. R., & Redman, M. P. 1995, *MNRAS*, 277, 700
- Felli, M., Churchwell, E., Wilson, T. L., & Taylor, G. B. 1993, *A&AS*, 98, 137
- Franco, J., Shore, S. N., & Tenorio-Tagle, G. 1994, *ApJ*, 436, 795
- Franco, J., Tenorio-Tagle, G., & Bodenheimer, P. 1989, *RevMexAA*, 18, 65
- 1990, *ApJ*, 349, 126
- Franco, J., Kurtz, S., Hofner, P., Testi, L., García-Segura, G., & Martos, M. 2000, *ApJ*, 542, L143
- Garay, G. & Lizano, S. 1999, *PASP*, 111, 1049
- Garay, G., Rodríguez, L. F., Moran, J. M., & Churchwell, E. 1993, *ApJ*, 418, 368
- García-Segura, G., & Franco, J. 1996, *ApJ*, 469, 171, paper I
- Giveon, U., Becker, R. H., Helfand, D. J., & White, R. L. 2005, *AJ*, 129, 348
- Hollenbach, D., Johnstone, D., Lizano, S., & Shu, F. 1994, *ApJ*, 428, 654
- Kim, K.-T. & Koo, B.-C. 2001, *ApJ*, 549, 979
- Kurtz, S., Cesaroni, R., Churchwell, E., Hofner, P., & Walmsley, C. M. 2000, *Protostars & Planets IV*, ed. V. Mannings, A. P. Boss, & S. S. Russell, (Tucson: Univ. of Arizona Press), 299
- Kurtz, S., Churchwell, E., & Wood, D. O. S. 1994, *ApJS*, 91, 659

- Kurtz, S. E., Watson, A. M., Hofner, P., & Birgit, O. 1999, *ApJ*, 514, 232
- Lizano, S., Canó, J., Garay, G., & Hollenbach, D. 1996, *ApJ*, 468, 739
- Mac Low, M.-M., Van Buren, D., Wood, D. O. S., & Churchwell, E. 1991, *ApJ*, 369, 395
- Mezger, P. G., Altenhoff, W., Schraml, J., Burke, B. F., Reifstein, E. C. III, & Wilson, T. L. 1967, *ApJ*, 150, L157
- Osterbrock, D. E. 1989, *“Astrophysics of Gaseous Nebulae and Active Galactic Nuclei”*, (Mill Valley: University Science Books)
- Richling, S., & Yorke, H. W. 1997, *A&A*, 327, 317
- Sewilo, M., Churchwell, E., Kurtz, S., Goss, W. M., & Hofner, P. 2004, *ApJ*, 605, 285
- Spitzer, L. 1954, *ApJ*, 120, 1
- Stone, J. M., & Norman, M. L. 1992, *ApJS*, 80, 753
- Strömgren, B. 1939, *ApJ*, 89, 526
- Tenorio-Tagle, G. 1979, *A&A*, 71, 59
- Van Buren, D., & Mac Low, M.-M. 1992, *ApJ*, 394, 534
- Van Buren, D., Mac Low, M.-M., Wood, D.O.S., & Churchwell, E. 1990, *ApJ*, 353, 570
- Van Buren, D., & McCray, R. 1988, *ApJ*, 329, L93
- Walsh, A. J., Burton, M. G., Hyland, A. R., & Robinson, G. 1998, *MNRAS*, 301, 640
- Williams, R. J. R. 2002, *MNRAS*, 331, 693
- Williams, R. J. R., Ward-Thompson, D., & Whitworth, A. P. 2001, *MNRAS*, 327, 788
- Wilson, T. L., & Jäger, B. 1987, *A&A*, 184, 291
- Wood, D. O. S., & Churchwell, E. 1989, *ApJS*, 69, 831
- Yorke, H. W., & Welz, A. 1996, *A&A*, 315, 555

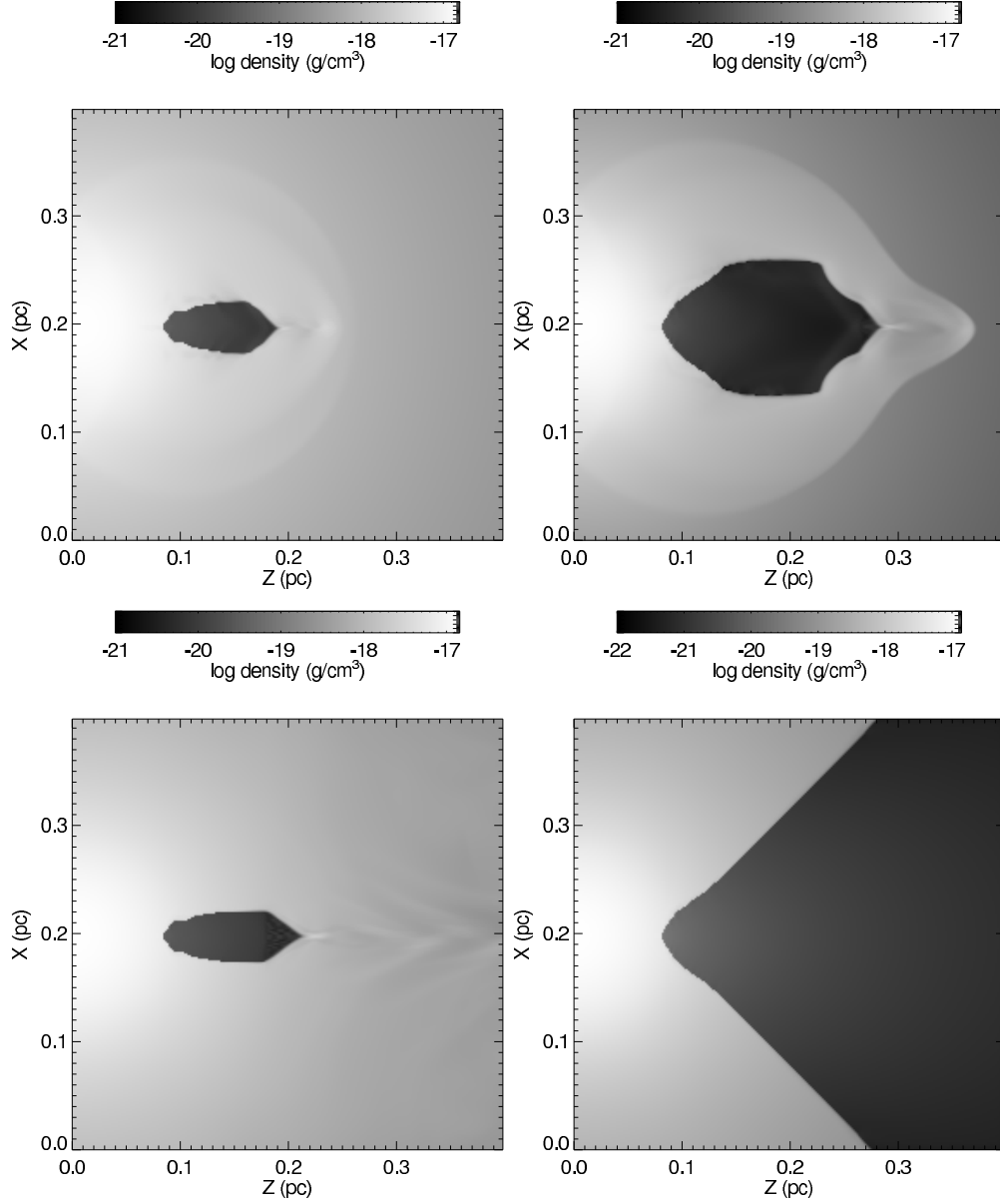


Fig. 1a.— Gas density snapshots of models A0 (left) and B0 (right). The star is located at the edge of the core, 0.1 pc from the core center:  $[(x, z)_\star = (0.2, 0.1)]$  while  $[(x, z)_{\text{core center}} = (0.2, 0.0)]$ . Times in years are  $t = 1 \times 10^5$  (top),  $t = 6 \times 10^5$  (bottom). Model A0 reaches pressure equilibrium, while model B0 produces a blister. For comparison, we note that a log density ( $\text{g cm}^{-3}$ ) of  $-19$  corresponds to number densities of  $3 \times 10^4 \text{ cm}^{-3}$  for molecular hydrogen and  $6 \times 10^4 \text{ cm}^{-3}$  for ionized hydrogen.

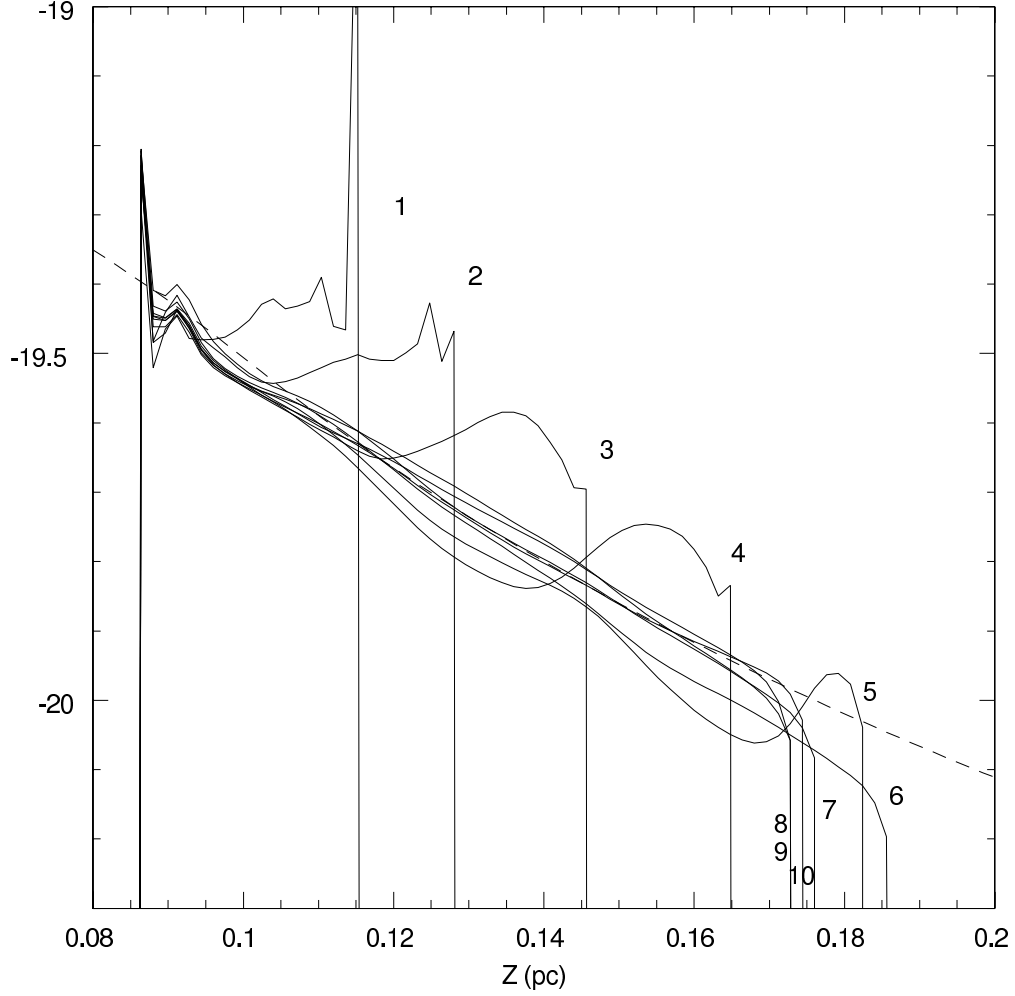


Fig. 1b.— Evolution of the photoionized gas density of model A0. Curves are labeled in units of 20,000 yr. That is, curves 1, 2, 3... correspond to times of 20, 40, 60... kilo years. The star is located at  $Z = 0.1$  pc. The short dashed line represents the initial density distribution divided by 200, which is the expected equilibrium value ( $\rho \propto r^{-2}$  for  $r \geq r_c$ ). The vertical axis shows log mass density in units of  $\text{g cm}^{-3}$ ; values Log mass densities of  $-19.5$  and  $-20$   $\text{g cm}^{-3}$  correspond to number densities of  $1.9 \times 10^4$  and  $6.0 \times 10^3 \text{ cm}^{-3}$ , respectively.



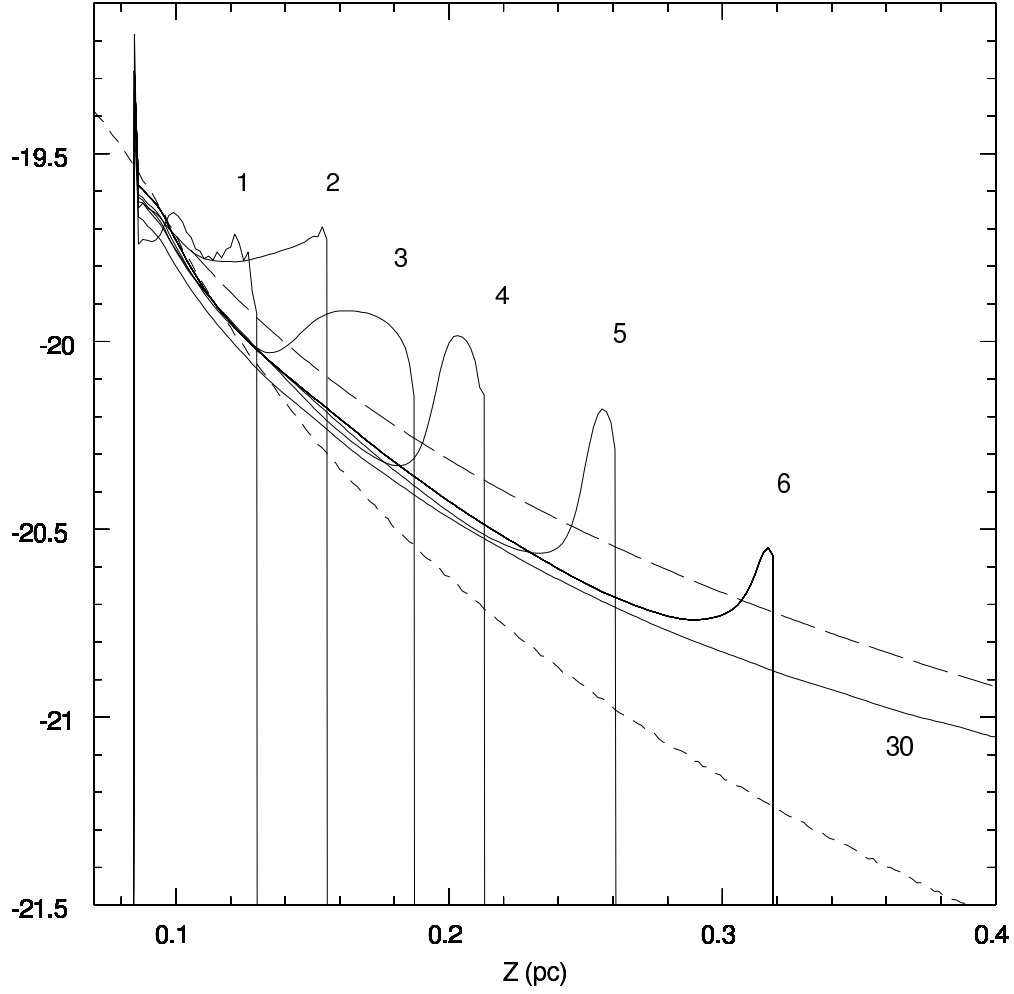


Fig. 1c.— Same as Figure 1b but for model B0. The curves labeled 1, 2, 3... correspond to times in multiples of 20,000 yr. The star is located at  $Z = 0.1$  pc. The short-dashed line represents the initial density structure divided by 200, which is the expected equilibrium value ( $\rho \propto r^{-3}$  for  $r \geq r_c$ ). The long-dashed line is an  $r^{-2}$  power law with the same central density. Log mass densities of  $-20$ ,  $-20.5$  and  $-21 \text{ g cm}^{-3}$  correspond to number densities of 6000, 1900, and  $600 \text{ cm}^{-3}$ , respectively.

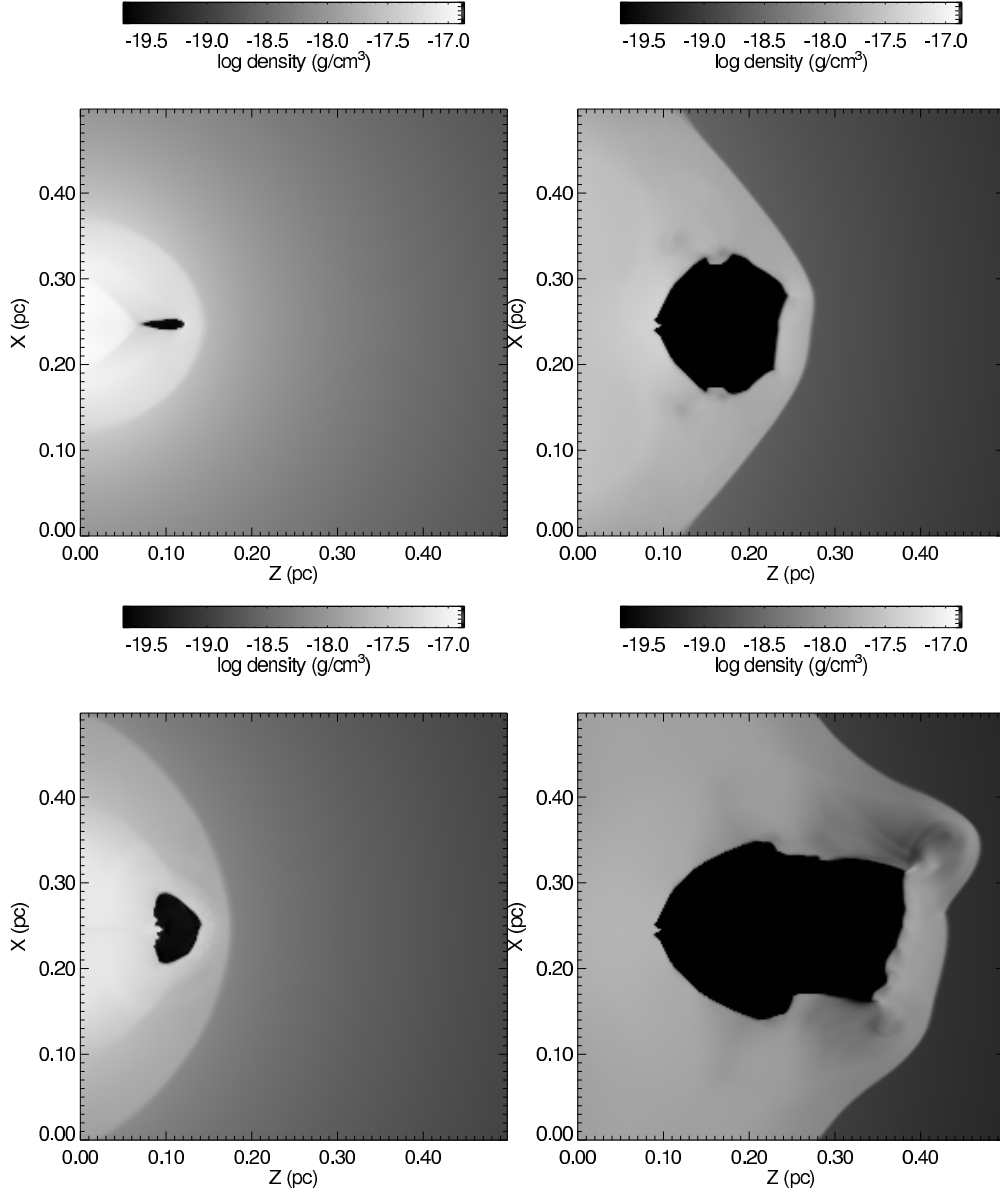


Fig. 2.— Gas density snapshots of model A2. Times in units of  $10^5$  years are 0.8 (top left), 1.6 (bottom left), 2.4 (top right), and 3.2 (bottom right). The star departs from the core center at  $t = 0$  with  $v_\star = 2 \text{ km s}^{-1}$ . X and Z coordinates are fixed to the star  $[(x, z)_\star = (0.25, 0.1)]$ , but the final stellar position is 0.65 pc from the starting point. This motion is represented in the model by the molecular core moving leftward, out of the figure. Log mass densities of  $-17$ ,  $-17.5$  and  $-18 \text{ g cm}^{-3}$  correspond to number densities of  $3 \times 10^6$ ,  $9.5 \times 10^5$ , and  $3 \times 10^5 \text{ cm}^{-3}$ , respectively, for the molecular gas.

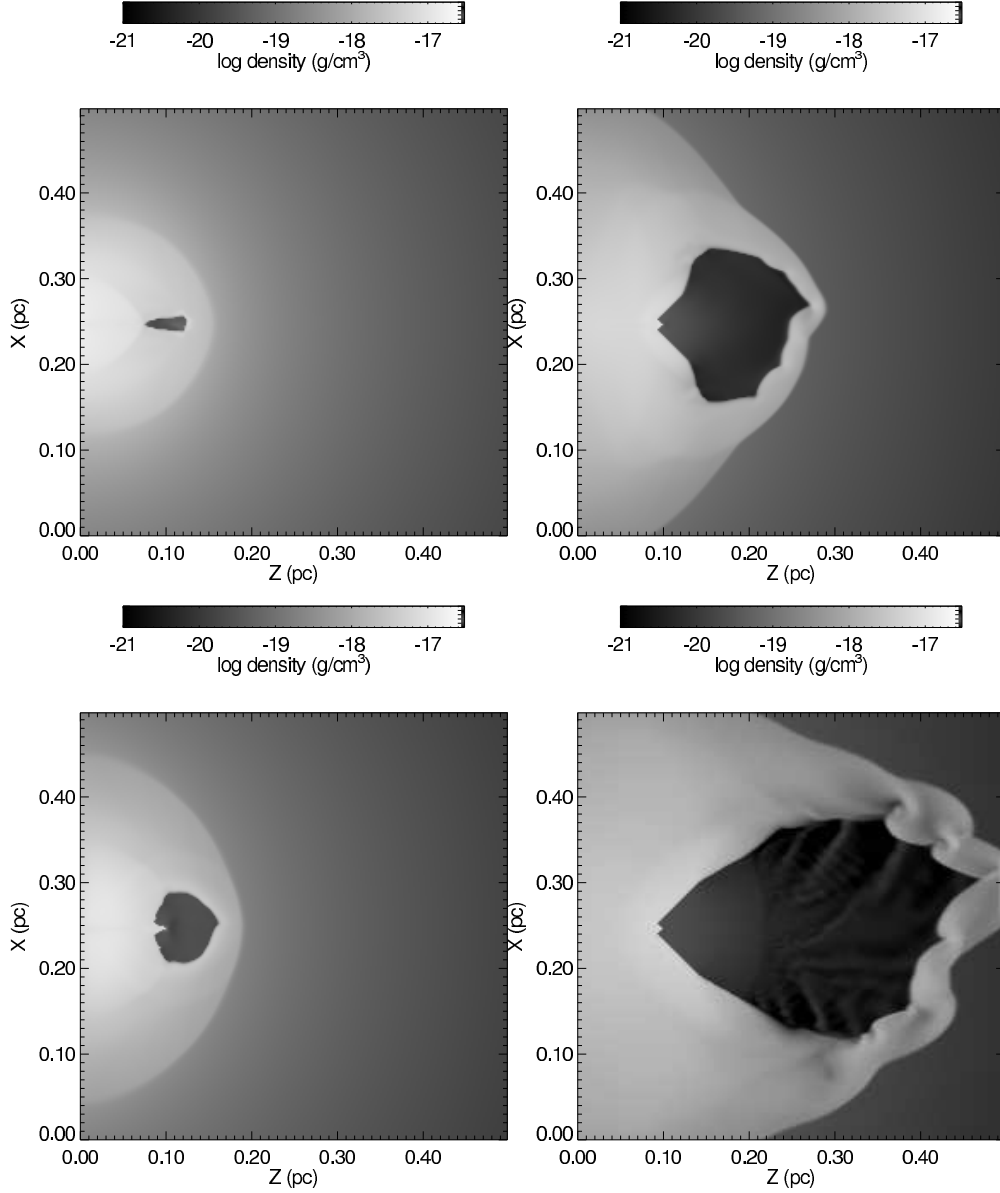


Fig. 3.— Gas density snapshots of model B2. Times in units of  $10^5$  years are 0.8 (top left), 1.2 (bottom left), 1.66 (top right), and 2 (bottom right). The star departs from the core center at  $t = 0$  with  $v_{\star} = 2 \text{ km s}^{-1}$ . X and Z coordinates are fixed to the star  $[(x, z)_{\star} = (0.25, 0.1)]$ . The final stellar position is 0.4 pc from the starting point. Because of the steeper density gradient, the expansion of the HII region in this model is more rapid than that shown in Figure 2; the final frame of Figure 3 is intermediate in time between the second and third frames of Figure 2.

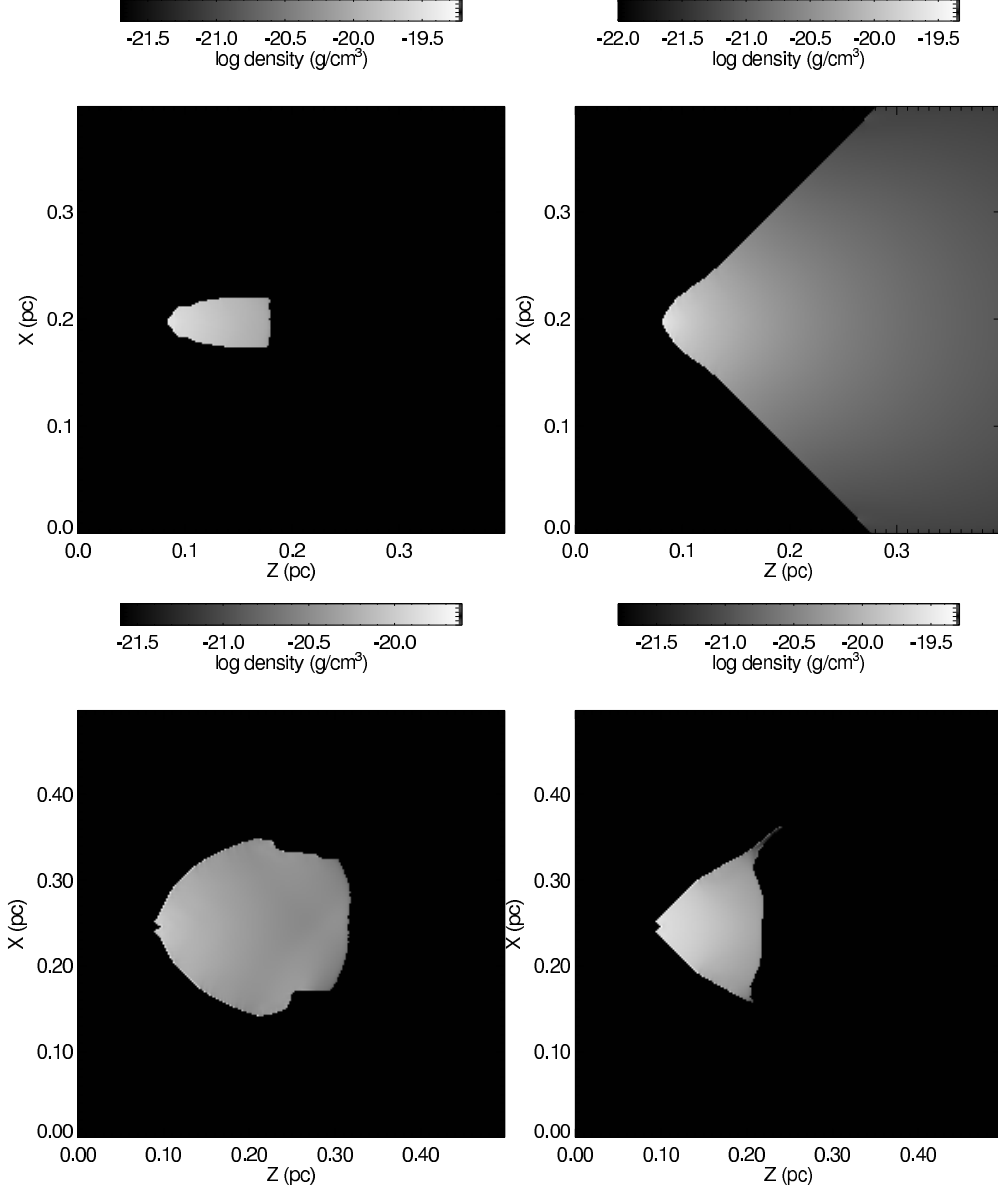


Fig. 4.— Final photoionized gas densities for models A0 (top left), B0 (top right), A2 (bottom left) and B2 (bottom right). Times correspond to the end times in Figure 1a ( $6 \times 10^5$  yr for A0 and B0), Figure 2 ( $3.2 \times 10^5$  yr for A2), and Figure 3 ( $2.0 \times 10^5$  yr for B2). A log mass density of  $-20$  corresponds to an electron density of  $6,000 \text{ cm}^{-3}$  for the ionized gas. Black areas show molecular gas and do not follow the log density gray-scale.

Fig. 5a.— Total gas density snapshots of models A8 (left panels) and A12 (right panels). Times in units of  $10^5$  years are (top to bottom): 0.12, 0.4, 0.64, 0.88, 1.12, 1.4, 1.64, 1.88 (for both models). The cloud core center is at  $[(x, z)_{core} = (0.1, 0.1)]$  on the first frame, and the simulation begins with the star on the left edge of the core, at initial position  $[(x, z)_{\star} = (-0.1, 0.1)]$ . As the simulation evolves, the star first moves toward the core center with  $v_{\star} = 8$  and  $12 \text{ km s}^{-1}$ , respectively. Eventually the star passes through the core and exits into the density ramp on the  $+z$  side of the core. The final  $X - Z$  stellar position corresponds to 1.535 pc and 2.3 pc, respectively, from the cloud center  $[(x, z)_{\star} = (0.1, 0.1)]$ .

Fig. 5b.— Photoionized gas density counterpart of Figure 5a.

Fig. 6a.— Total gas density snapshots of models B8 (left panels) and B12 (right panels). Times in units of  $10^5$  years are (top to bottom): 0.12, 0.28, 0.4, 0.52, 0.64, 0.76, 0.88, 1 (for both models). The cloud core center is at  $[(x, z)_{core} = (0.1, 0.1)]$  on the first frame, and the simulation begins with the star on the left edge of the core, at initial position  $[(x, z)_{\star} = (-0.1, 0.1)]$ . As the simulation evolves, the star first moves toward the core center with  $v_{\star} = 8$  and  $12 \text{ km s}^{-1}$ , respectively. Eventually the star passes through the core and exits into the density ramp on the  $+z$  side of the core. The final stellar position is 0.82 pc and 1.23 pc, respectively, from the starting position.

Fig. 6b.— Photoionized gas density counterpart of Figure 6a. Frames 4 (bottom of first column) and 11 (third frame of third column) illustrate the effect of the star overtaking a leading, piled-up clump of gas. This could result in either a core-halo morphology or an ultracompact HII region with extended emission. See §5.4 and figure 8.



Fig. 7.— Comparison of the famous central part of M16 (top) in  $H\alpha$  with model B8 at  $t = 8.8 \times 10^4$  yr (bottom). The bottom left frame shows the ionized gas density while the bottom right frame shows the total gas density. Although the model does not pretend to reproduce M16, the similarity is striking.

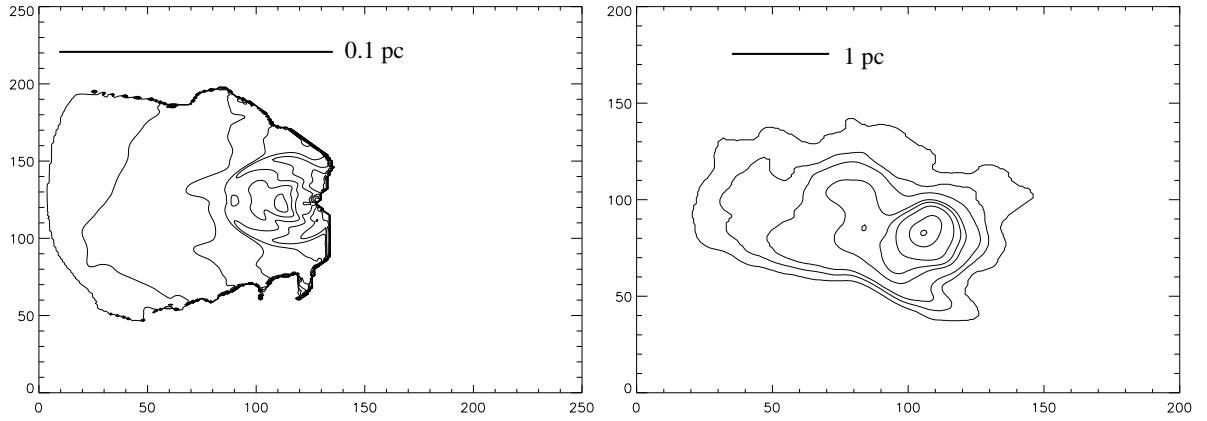


Fig. 8.— Comparison of the ionized gas density (squared) of model B12 with an image of G31.3–0.2. The contours of the left frame are proportional to  $n_e^2$  which in turn is proportional to the radio flux density in the case of optically thin emission. The right frame (adapted from Kurtz et al. 1999) shows the radio emission of G31.3–0.2, which has extended, lower density gas surrounding a compact, higher density component. The 1 pc size scale assumes a distance of 5.7 kpc. The model does not pretend to reproduce the detailed structure of G31.3–0.2, but rather is intended to show that the self-blocking effect can give rise, at least on small scales, to the morphology of a UC H II region with extended emission.

Table 1. Model Attributes

| Model | $V_{\star}$<br>km s <sup>-1</sup> | Halo Density<br>Gradient | Grid scale<br>pc | Lifetime as<br>UC HII (10 <sup>5</sup> yr) | Lifetime as Cometary<br>UC HII (10 <sup>4</sup> yr) |
|-------|-----------------------------------|--------------------------|------------------|--------------------------------------------|-----------------------------------------------------|
| A0    | 0                                 | $r^{-2}$                 | 0.4              | $\infty$                                   | 0                                                   |
| B0    | 0                                 | $r^{-3}$                 | 0.4              | 0.8                                        | 0                                                   |
| A2    | 2                                 | $r^{-2}$                 | 0.5              | 2.0                                        | 8                                                   |
| B2    | 2                                 | $r^{-3}$                 | 0.5              | 1.4                                        | 8                                                   |
| A8    | 8                                 | $r^{-2}$                 | 0.2              | 0.64                                       | 6.4                                                 |
| B8    | 8                                 | $r^{-3}$                 | 0.2              | 0.4                                        | 4                                                   |
| A12   | 12                                | $r^{-2}$                 | 0.2              | 0.64                                       | 6.4                                                 |
| B12   | 12                                | $r^{-3}$                 | 0.2              | 0.4                                        | 4                                                   |

This figure "fig5a.png" is available in "png" format from:

<http://arxiv.org/ps/astro-ph/0508467v1>

This figure "fig5b.png" is available in "png" format from:

<http://arxiv.org/ps/astro-ph/0508467v1>

This figure "fig6a.png" is available in "png" format from:

<http://arxiv.org/ps/astro-ph/0508467v1>

This figure "fig6b.png" is available in "png" format from:

<http://arxiv.org/ps/astro-ph/0508467v1>

This figure "fig7.png" is available in "png" format from:

<http://arxiv.org/ps/astro-ph/0508467v1>